CRYSTAL GROWTH & DESIGN

Article

pubs.acs.org/crystal

Mechanism of Rare Earth Incorporation and Crystal Growth of Rare Earth Containing Type-I Clathrates

Andrey Prokofiev,*[,†] Robert Svagera,[†] Monika Waas,[†] Matthias Weil,[‡] Johannes Bernardi,[§] and Silke Paschen[†]

[†]Institute of Solid State Physics, Vienna University of Technology, Wiedner Hauptstrasse 8-10, Vienna 1040, Austria

[‡]Institute of Chemical Technologies and Analytics, Vienna University of Technology, Getreidemarkt 9/164-SC, 1060 Vienna, Austria

[§]USTEM, Wiedner Hauptstrasse 8-10, Vienna 1040 Austria

Supporting Information

ABSTRACT: Type-I clathrates possess extremely low thermal conductivities, a property that makes them promising materials for thermoelectric applications. The incorporation of cerium into one such clathrate has recently been shown to lead to a drastic enhancement of the thermopower, another property determining the thermoelectric efficiency. Here we explore the mechanism of the incorporation of rare earth elements into type-I clathrates. Our investigation of the crystal growth and the composition of the phase $Ba_{8-x}RE_xTM_ySi_{46-y}$ (RE = rare earth element; TM = Au, Pd, Pt) reveals that the RE content x is mainly governed by two factors, the free cage space and the electron balance.

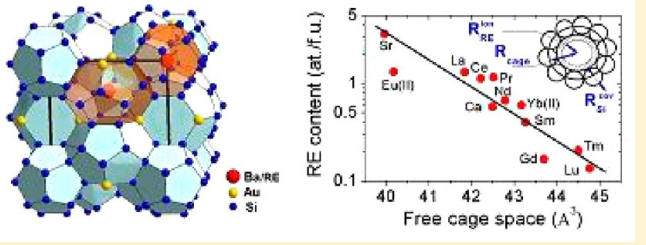

INTRODUCTION

In order to make thermoelectric materials economically viable, a drastic increase in their efficiency should be achieved. Two approaches aim at increasing the thermoelectric efficiency: the maximization of the power factor and the minimization of the thermal conductivity.[1] The combination of both strategies in a single material is the most promising way to high thermoelectric performance.

Clathrates are materials with intrinsically low lattice thermal conductivity. This is attributed to special features of the crystal structure (e.g., Figure 1 for the prototypical type-I clathrate $Ba_8Au_6Si_{40}$).

The clathrate framework is composed of tetrahedrally bound silicon, germanium, or tin (tetrel) atoms partially substituted by atoms of a lower valence (electron acceptors) for phase stabilization. The framework forms large cavities or cages that are occupied by large electropositive atoms (e.g., alkaline or heavy alkaline earth metals). The encapsulated atoms in the oversized cages are weakly bound to the framework atoms. The interaction of heat carrying acoustic phonons propagating through the framework with strongly anharmonic vibrations of the encapsulated atoms (rattlers) results in low thermal conductivity.[2−4] The power factor has been maximized over the past few years by optimizing the charge carrier concentration through tuning the framework composition; thus the dimensionless thermoelectric figure of merit ZT characterizing the total efficiency reaches now 1.63 for n-type $Ba_8Ga_{16-x}Ge_{30+x}$ at 1100 K and 1.1 for p-type $Ba_8Ga_{16+x}Ge_{30-x}$ at 900 K.[5,6] Band structure engineering may increase the power factor of clathrates even beyond the charge carrier concentration optimized values. One of the possibilities was suggested to be the incorporation of an appropriate rare earth (RE) element.[7]

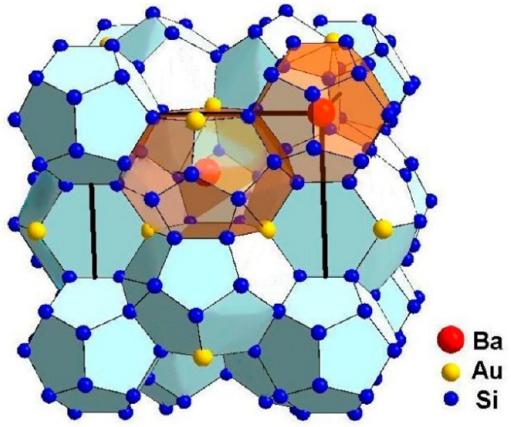

Figure 1. Structure of the type-I clathrate $Ba_8Au_6Si_{40}$. One larger and one smaller cage are shown as red-shaded polyhedra.

Indeed, by the incorporation of Ce into type-I clathrate cages, the thermopower was recently demonstrated to be enhanced by about 50% over the value of the Ce-free reference material with the same charge carrier concentration.[8] This enhancement was attributed to electron correlation effects (the

Received: April 3, 2015
Revised: December 2, 2015
Published: December 2, 2015

DOI: 10.1021/acs.cgd.5b00461
Cryst. Growth Des. 2016, 16, 25−33

Kondo interaction) enhanced by the rattling of Ce in the cages. The Kondo temperature, characterizing the energy scale of the electron correlations, appeared to be shifted from about 1 K at low temperature to about 800 K at high temperature when the rattling modes are activated. Thus, rattling in this Ce-containing clathrate is the origin of both the reduced thermal conductivity and the enhanced thermopower, making correlated clathrates an attractive object for further investigations.

In the above work,[8] a Ce and La content of about 1 atom per formula unit was reached. Both RE atoms were shown to occupy the 2*a* site in the smaller of the two cages. The only partial (about a half) occupancy of this site leads to disorder in the Kondo lattice and thus strongly reduces the electron mobility, which adversely affects the thermoelectric performance. Thus, in the present work, we study factors determining the RE cage incorporation and crystal growth conditions providing the maximal content of RE in clathrates. In the first part of the paper, we investigate which composition of the parent clathrate phase is optimal for a maximal incorporation of RE elements and the best thermodynamic conditions for crystallization of this phase. In the second part, on the basis of this study, we develop the optimal crystal growth technique. Finally, we study the mechanism of the RE incorporation by exploring trends across the whole RE series.

EXPERIMENTAL SECTION

Synthesis. Polycrystalline samples were synthesized by melting Ba, the selected RE (or alkali earth) element, the selected TM element and Si (or Ge) in a horizontal water cooled copper boat in argon atmosphere (6N) using high frequency heating. At least three remeltings were done for sample homogenization. The typical weight of polycrystalline samples for analytical investigations was about 1 g and for single crystal preparation 15−20 g. The purity of the starting materials was 99.99% for La and Ce, 99.9% for other RE elements, 99.5% for Ba, Sr, and Ca, 99.95% for Au, Pd, and Pt, 99.9999% for Si, and 99.999% for Ge. All operations (weighing, cleaning the surface of air sensitive metals by polishing) were carried out in an MBraun glovebox with argon atmosphere (6N). Single crystal growth was performed by a floating zone technique using optical heating in a four mirror furnace (Crystal Corporation). All steps were done under Ar 6N protective atmosphere.

X-ray Analysis. Single crystal X-ray diffraction data collections were performed at room temperature on a Bruker APEX-II four-circle diffractometer for the Ce, Pr, and Sm compounds and on a Bruker SMART three-circle diffractometer for the Yb compound. For all crystals complete reciprocal spheres with high redundancy were measured with laboratory Mo−Kα radiation. Absorption correction for each data set was based on the "multiscan" approach with the program SADABS;[9] correction for extinction was performed with the SHELXL-97 program.[10]

The structures were refined with the SHELXL-97 program using the coordinates of previously reported clathrate compounds of similar composition. For modeling the site occupancies due to replacement of Ba with an RE element on the 2*a* site, of Au with Si on the 6*c* site and of Si with Au on the 24*k* site, the corresponding atom pairs were refined with common coordinates and common anisotropic displacement parameters. Laue images were taken with a Photonic Science Digital Laue camera and analyzed with the program Orient Express.[11]

Powder XRD data were collected using a Siemens D5000 diffractometer with Cu−$K_{\alpha 1,2}$ radiation at room temperature. The phase analysis and the Rietveld refinement were carried out using the software PANalytical HighScore Plus package.[12]

SEM/EDX. Polished cross sections of the samples were investigated by scanning electron microscopy with energy dispersive X-ray analysis (SEM/EDX) using an EDAX New XL-30 135-10 UTW+ detector and with wavelength dispersive X-ray analysis (SEM/WDX) using a Microspec WDX-600. Both X-ray analytical systems are attached to a Philips XL30 ESEM. All investigated samples were excited by 30 keV electrons to ensure proper excitation of Au L shells. As the energy differences between the L X-ray emission lines of Ba and Ce are small, the line broadening from the EDX detection system leads to line overlaps which have to be separated by the curve fitting algorithm included in evaluation software. The whole data reduction of the EDX spectra and quantitative analysis were done by the EDX Control Software (from EDAX Inc.) supplied by the manufacturer of the detector system. To reduce the detector induced line broadening, the amplifier time of the detector system was set to 100 μs which reduces the allowed maximum count-rate as well. The statistical error was limited by increasing the acquisition time up to 900 s per spectrum. To avoid carbonaceous contamination of the sample surface due to long exposure of the sample surface to the beam, we prefer to scan areas of typically 10 μm × 10 μm, but we had to select spot measurements as well in small areas of interest. Since rather low RE contents had to be measured the question of the sensitivity of the technique arose. In order to test it, we allowed the EDX evaluation program to compute the Ce content in a Ce-free clathrate sample. An amount of 0.1−0.3 atom % (0.05−0.15 atoms per formula unit) was determined in this phase. This value indicates the RE zero-level of the EDX measurement. With the above measurement parameters, based on statistical evaluation of the data, the measured element contents have the following relative uncertainties (%): Ba-1, Au-2, Si-0.3, La-6, Ce-4, Pr-3, Yb-3, Sm-7.

The accuracy of our EDX measurements was checked using a reference single phase single crystalline clathrate sample whose composition was determined by the inductively coupled plasma mass spectrometry (ICP-MS). The analysis was carried out at the Max Planck Institute for Chemical Physics of Solids (Dresden, Germany). The comparison between the EDX and ICP-MS compositions yielded very good agreement (Supporting Information).

Electron Backscatter Diffraction (EBSD). EBSD measurements were done with an EDAX DigiView EBSD camera attached to a FEI Quanta 200 field emission gun SEM. As EBSD diffraction patterns (Kikuchi bands) are formed in a region close to the sample surface (up to 50 nm depth), strain and contamination lead to the loss of the diffraction pattern contrast. Therefore, in addition to the standard preparation steps of grinding and polishing, EBSD investigation required a 10−30 min polishing with 0.05 μm colloidal silica and final plasma cleaning.

Details of the crystal structure investigations may be obtained from FIZ Karlsruhe, 76344 Eggenstein-Leopoldshafen, Germany (fax: (+49)7247-808-666; e-mail: crysdata@fiz-karlsruhe.de), on quoting the deposition numbers CSD-430170 for the Ce-compound, CSD-430171 for the Pr-compound, CSD-430172 for the Sm-compound, and CSD-430173 for the Yb-compound. CCDC 1441433−1441436 contains the supplementary crystallographic data for this paper.

RESULTS AND DISCUSSION

Search for Parent Clathrate Phase for RE Element Substitution. Clathrates are Zintl-phases, i.e., polar intermetallic phases whose stability and properties are governed by the zero-sum balance between donated and accepted electrons. The majority of clathrates adopt the composition nearly corresponding the case when electrons donated by the electropositive guest atoms are fully used up by the more electronegative framework acceptor atoms for the fulfillment of their covalent bond requirements. The latter thus become anions and behave as pseudotetrel atoms with their four valence electrons.[13,14] Thus, the valence electrons of the guest atoms must be accepted by the host atoms. As each host atom is 4-fold bonded to other host atoms, this can be accomplished by selecting guest and host atoms of appropriate valence. The general formula of the prototypical type-I clathrate is $G^{II}_{8}H^{v}_{y}H^{IV}_{46-y}$, where G^{II} denotes a divalent (e.g., alkaline earth) guest atom, H^{IV} a four valent (group 14) host atom, and

DOI: 10.1021/acs.cgd.5b00461
Cryst. Growth Des. 2016, 16, 25−33

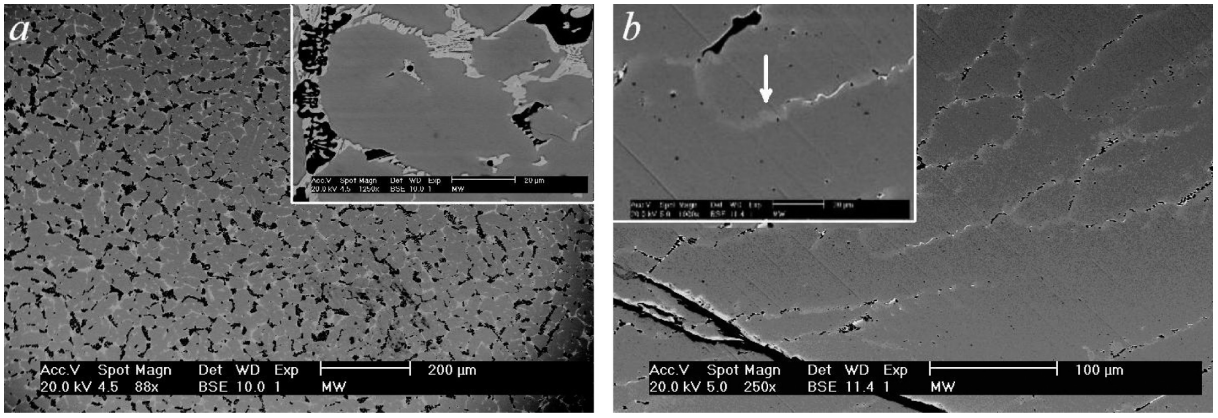

Figure 2. SEM images of (a) the as-cast sample obtained from the starting composition $Ba_6Ce_2Au_6Si_{40}$ and (b) the sample with Ph3, in which areas with diffuse boundaries are seen (arrow in inset).

H^v a host atom of a lower valence ($v < 4$) which serves as acceptor for the electrons donated by the guest atom. With all valence electrons used up (which is the case if $2{\cdot}8 = (4\text{-}v){\cdot}y$) an electrical insulator is expected. Real clathrates are typically degenerate semiconductors; this is attributed to slight deviations from the above oversimplified situation, e.g., due to off-stoichiometry, defects, or incomplete charge transfer. In some clathrates, this deviation can be rather large, e.g., $Ba_8Au_6Si_{40}$,[15] K_8Si_{46}.[16]

Since the substitution of divalent Ba by trivalent Ce leads to an increase of the number of donated electrons (>16 per formula unit), it must be accompanied by an enhancement of the acceptor capacitance of the framework $(4\text{-}v){\cdot}y$. Therefore, we searched for parent clathrate phases that contain acceptors of particularly low valence v. The noble transition metals (TM) Au with valence one and Pt and Pd with valence zero seemed to be the best candidates. In addition, the achievable TM content y must be large to accomplish $(4\text{-}v){\cdot}y > 16$. The phase $Ba_8Au_ySi_{46-y}$ (BAS) forms in a wide Au concentration range $2.2 < y < 6.1$.[15,17] At $y = 6$, full electron balance according to the Zintl rule corresponds to two Ce atoms per formula unit. This may be denoted as $Ba^{2+}{}_6Ce^{3+}{}_2Au^{3-}{}_6Si^{0}{}_{40}$, where the superscripts correspond to the formal charge after the electron transfer. From the reported composition ranges $2.5 \leq y \leq 4.1$ for $Ba_8Pd_ySi_{46-y}$ and $2.8 \leq y \leq 4.9$ for $Ba_8Pt_ySi_{46-y}$[18] the Pt case is thus more promising than the Pd one. These three phases $Ba_8TM_ySi_{46-y}$ (TM = Au, Pd, Pt) were selected as starting materials for the Ce substitution.

Solubility of Ce in $Ba_8TM_ySi_{46-y}$. Samples of the nominal composition $Ba_6Ce_2TM_6Si_{40}$ (TM = Au, Pt, Pd) were obtained by high frequency melting the elements in a water-cooled copper crucible (The synthesis with TM = Au was already reported in ref 8.)

According to X-ray powder diffraction (XRD), all three as-cast products are polyphased (Figure 2a), with the clathrate phase as the main phase. Si- and Ce-rich phases are secondary phases, the stoichiometry of the latter being different for various TM elements (Supporting Information). The resulting compositions of the clathrate phases determined by EDX as well as the secondary Ce-containing phases are given in Table 1.

In the Au and Pt clathrate phases $Ba_{8-x}Ce_xTM_ySi_{46-y}$, Ce was detected in amounts of $x = 0.65$ and 0.22, respectively.

This is smaller than the starting Ce content of $x = 2$. The Ce content in the Pd-containing clathrate is lower than the detection level of EDX (Table 1). The Ce level correlates with the acceptor capacity of the framework $(4\text{-}v){\cdot}y$, which is maximal (17.16) in the Au clathrate phase and below 16 in the Pt and the Pd phases (15.56 and 14.92, respectively).

Table 1. EDX Compositions of the Clathrate Phases Obtained from the Starting Compositions $Ba_6Ce_2TM_6Si_{40}$ (TM = Au, Pt, Pd) (at./f.u.) and Ce-Containing Secondary Phases

TM =	Au	Pt	Pd
Ba	7.61	7.72	7.78
Ce x =	0.65	0.22	0.0
TM y =	5.72	3.89	3.73
Si	40.01	42.17	42.50
Ce-containing secondary phases	$CeAu_2Si_2$, Ce_2AuSi_3[19,20]	$CePtSi_3$[21]	$Ce_2Pd_3Si_5$[22]

The synthesis of the Ce-containing clathrate phase, $Ba_6Ce_2Au_4Si_{42}$, with a Au content of $y = 4$ was first claimed[23] but later acknowledged to be the overall composition of polyphased material with Ce only present in a nonclathrate phase.[24,25]

Apparently, the Au content $y = 4$ was too low for the incorporation of Ce. Since we found the highest Ce content in the Au clathrate phase, we focused our further efforts on this phase.

Having established the existence of Ce containing clathrate phases one faces the task to isolate them in phase pure form. To prepare a single phase clathrate starting from the above EDX composition of the clathrate phase (Table 1 and Ph1 in Table 2) seemed at the first glance a promising route. However, the product of the new synthesis was again multiphased material with the Ce content in the main clathrate phase reduced to $x = 0.27$ (Ph2, Table 2).

The third synthesis with the starting composition of Ph2 yielded a clathrate phase without any detectable Ce content (phase Ph3, Table 2). Table 2 summarizes the results of these successive syntheses. Thus, the Ce substitution limit depends on the starting conditions.

For a better understanding of the phase relations in the Ba–Ce–Au–Si system, we investigated the final sample of the series (with Ph3) in more detail. Figure 2b shows the SEM image of the polished surface of this sample. According to XRD and EDX, the main phase is a Ce-free clathrate phase. A characteristic feature of the microstructure are light areas (higher intensity of backscattered electrons) having no distinct

DOI: 10.1021/acs.cgd.5b00461
Cryst. Growth Des. 2016, 16, 25–33

Table 2. Compositions (at./f.u.) of the $Ba_{8-x}Ce_xAu_ySi_{46-y}$ Phases in the Course of Successive Attempts to Isolate the Clathrate in Phase Pure Form[a]

	starting composition	clathrate phase Ph1	starting composition (same as Ph1)	clathrate phase Ph2	starting composition (same as Ph2)	clathrate phase Ph3
Ba	6.00	7.61	7.61	7.40	7.40	7.65
Ce	2.00	0.65	0.65	0.27	0.27	0.0
Au	6.00	5.72	5.72	5.18	5.18	5.08
Si	40.00	40.01	40.01	40.58	40.58	41.37

[a]The EDX compositions of the phases Ph1 and Ph2 were used as starting compositions for the synthesis yielding the clathrate phases Ph2 and Ph3, respectively.

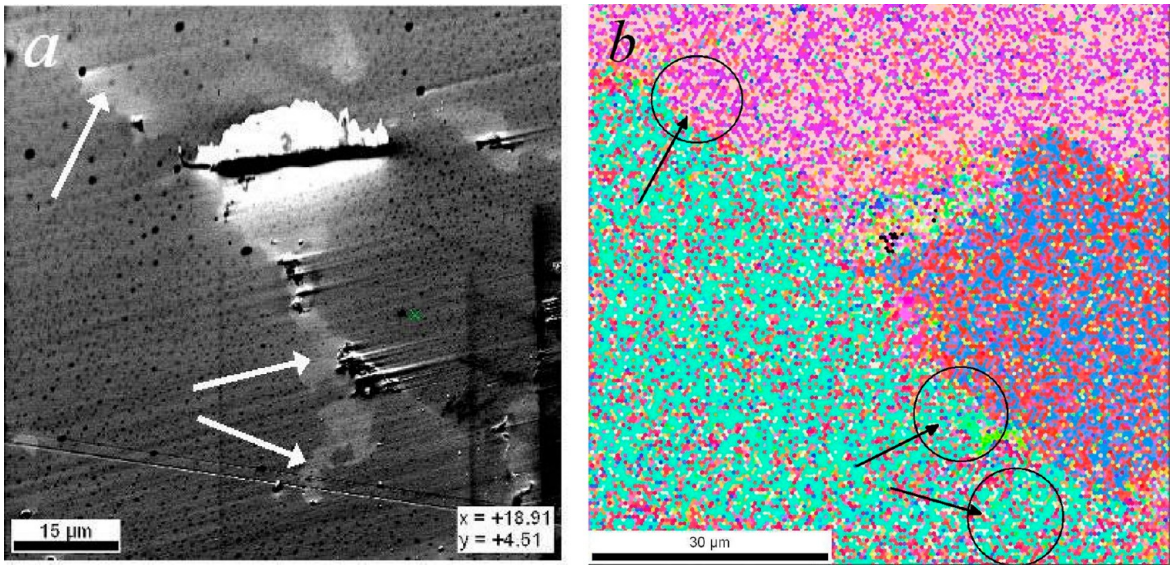

Figure 3. (a) Magnified part of sample with Ph3 (the arrows show Ce-enriched areas). (b) EBSD orientation map of the same area as in a).

boundaries with the large clathrate grains (see arrow in inset of Figure 2b and arrows in Figure 3a). Within these areas small black Si inclusions and white inclusions of a Ce-rich phase with sharp boundaries are seen (inset of Figure 2b). Our EDX analysis of the light areas away from the inclusions revealed that they are clathrate phases with a Ce content of $x = 0.81$. For the exact microscopic phase identification of these areas, we used EBSD orientation mapping.

Figure 3a,b shows the SEM and the EBSD images of the same area. According to EBSD, the Ce-rich light areas have the same crystal structure and even the same orientation as the adjacent large grains of the Ce-free material. From this observation the following scenario of the crystallization emerges. In the initial stage of the crystallization process, the clathrate phase repels Ce. As the growth proceeds, the intergrain melt gets enriched in Ce. After exceeding a critical concentration in the melt, Ce begins to be incorporated into the clathrate phase. The presence of Au-rich phases between large clathrate grains indicates that the melt is also enriched in Au as the crystallization proceeds.

Thus, relevant for the formation of the Ce-containing type-I clathrate phase is its relative stability with respect to competing nearest neighbor phases: the Ce-free clathrate, the elementary Si, $CeAu_{2-x}Si_{2+x}$ and the tetragonal Ce_2AuSi_3.

Correlations between Ce and Other Constituting Elements in the $Ba_{8-x}Ce_xAu_ySi_{46-y}$ Phase. The inhomogeneous samples with gradually varying cerium content (see, e.g., Figures 2b and 3a) provide the opportunity to systematically study the element relationships in a wide composition range and thus to trace the compositional response of the clathrate phase to Ce substitution. For this purpose, we investigated correlations between the local Ce content and the contents of other constituting elements at the same place measured by EDX. To improve the statistics and broaden the composition range, we prepared several additional $Ba_{8-x}Ce_xAu_ySi_{46-y}$ samples from the starting compositions listed in Table 3. Also a Ce-free clathrate sample was investigated for comparison.

Table 3. Starting Compositions (at./f.u.) of Samples 1−7

sample	Ba	Ce	Au	Si
1	7.88		6.85	39.31
2	7.40	0.27	4.75	41.58
3[a]	7.40	0.27	4.75	41.58
4	6.00	2.00	6.00	40.00
5	5.83	2.05	6.86	39.31
6	4.81	2.81	7.51	38.88
7	3.35	5.78	7.78	37.10

[a]2 and 3 are different samples with the same starting composition.

The samples were not annealed; i.e., the investigated compositions refer to clathrate crystallites formed directly from the melt. We assume that on formation from the melt a phase having many compositional degrees of freedom (e.g., Ba↔Ce or Au↔Si) adopts the composition that corresponds to the maximal phase stability.

DOI: 10.1021/acs.cgd.5b00461
Cryst. Growth Des. 2016, 16, 25−33

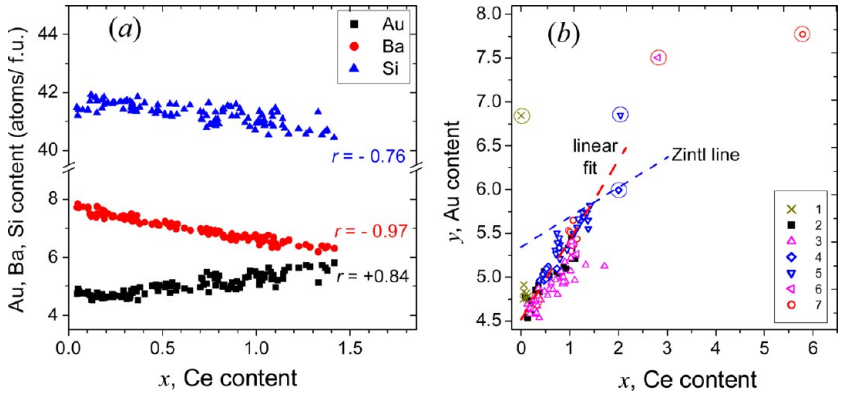

Figure 4. (a) Overall local Si, Ba, and Au contents vs local Ce content of the clathrate phase in samples 1−7 (Table 3) (r is the Pearson correlation coefficients); (b) relationship between the Au and Ce contents in more detail: Local clathrate phase compositions referring to different samples are shown by different symbols. The starting compositions of samples 1−7 are shown as group symbols inscribed in circles.

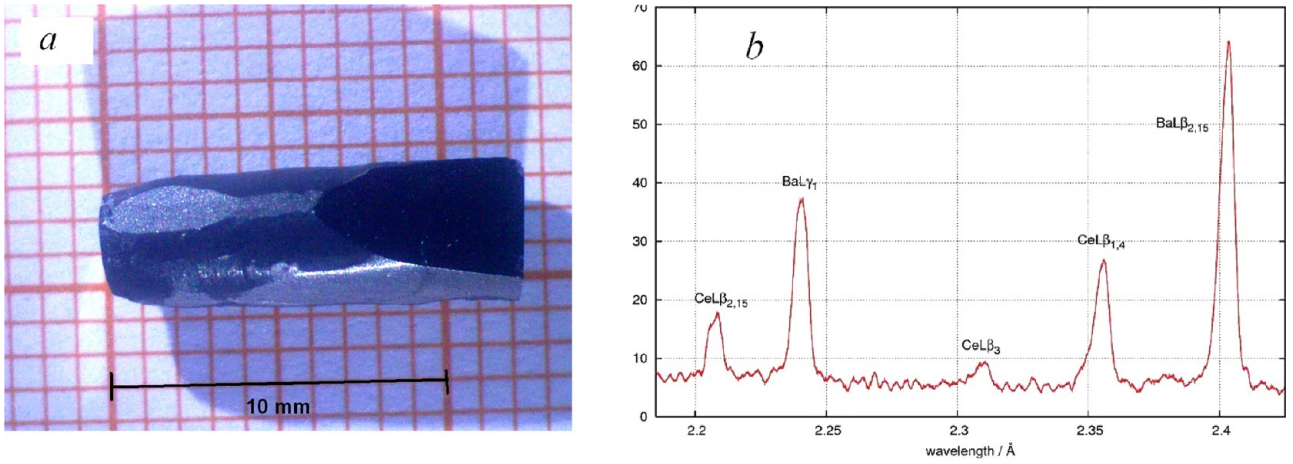

Figure 5. (a) Single crystal of a Ce-containing clathrate. (b) WDX spectrum of the crystal.

Figure 4a shows the Ba-, Au- and Si-contents as a function of the Ce-content. Despite some data scattering, correlations are clearly visible. The strength of a linear correlation between two variables can be characterized by the Pearson correlation coefficient r. It can vary from −1 (rigid anticorrelation) via 0 (no correlation) to 1 (rigid correlation). Ba−Ce, Au−Ce, and Si−Ce linear correlations have r = −0.97, +0.84, and −0.76, respectively. There is also a linear correlation between Au and Si (not shown), with r = −0.96. The high absolute r-value for the Ba−Ce (Au−Si) (anti)correlation is due to the obvious fact that Ba and Ce (Au and Si) occupy the same crystallographic sites, namely, 2*a* and 6*d* (6*c* for Au−Si). By contrast, Ce and Au occupy different sites; their correlation apparently stems from the Zintl rule.

In Figure 4b the measured Au−Ce dependence is shown in more detail; the local compositions of different samples are specified by different symbols. The corresponding starting compositions of these samples are shown as the group symbol in a circle. Despite the very different starting (melt) compositions, lying sometimes far from the solid phase compositions, the data points clearly group around a straight line. This indicates that the Au to Ce ratio, unlike the absolute Ce content, is an intrinsic property of the solid phase, weakly depending on the phase formation circumstances. As the figure shows, Ce cannot be found in $Ba_{8-x}Ce_xAu_ySi_{46-y}$ phases with y < 4.5. A linear fit of $y(x)$ yields $y = 0.73x + 4.5$, in qualitative agreement with the Zintl rule. However, a strict adherence to this rule would yield $y = 0.33x + 5.33$.

The larger linear factor (0.73 against 0.33) could be interpreted as a smaller than expected acceptor ability of the framework or, alternatively, as a larger than expected electron transfer from the guest atoms. However, a single-reason explanation of this deviation is hardly possible, since the observed smaller intercept indicates in each case the opposite effect. The relevant reasons of the observed deviation could be vacancies in the framework which act as electron acceptors or the valence of Au which is larger than 1. A remarkable amount of vacancies was not confirmed by X-ray and composition studies. Furthermore, our consideration is based on the Zintl concept which implies a fully ionic guest-framework bond. However, theoretical studies call this into question.[26,27] Finally, we have assumed charge balance, i.e., a charge carrier concentration per formula unit (f.u.) n = 0. In reality, n is finite. For instance, as it was determined by the Hall measurements in ref 8, $Ba_7Ce_1Au_{5.5}Si_{40.5}$ has 0.8 electrons/f.u., $Ba_{6.8}La_{1.23}Au_{5.9}Si_{40.1}$ 0.3 holes/f.u., both at room temperature. This misbalance, however, is too little to entirely explain the discrepancy. Thus, the deviation from the ideal Zintl behavior should be a subject of a separate investigation.

Crystal Growth of Some RE Containing Clathrates. Thus, a Ce-containing clathrate phase is only formed from a melt with a substantial Ce excess. On the other hand, an enhanced Au content facilitates the incorporation of Ce into

DOI: 10.1021/acs.cgd.5b00461
Cryst. Growth Des. 2016, 16, 25−33

the cages (Figure 4b). Thus, both Ce and Au should be present in excess in the starting melt. This provides the basis for the development of a synthesis technique for a single phase Ce-containing clathrate. To obtain a macroscopic single phase sample the microscopic process discussed above for Ce-containing clathrate areas in polyphased samples has to be scaled up. With this aim, we carried out a controlled crystallization from the off-stoichiometric melt using a floating zone technique in a mirror furnace.

The composition of the feed rod was optimized to $Ba_{5.82}Ce_{2.04}Au_{6.85}Si_{39.29}$, which corresponds to starting composition 5 of Table 3 yielding the highest Ce content (see Figure 4b). For a stable growth the pulling rate should not exceed 0.3 mm/h. An even larger Ce and Au excess was tested, but it leads to a crystal growth instability. Single crystals of up to 200 mm^3 could be grown (Figure 5a).

We applied this technique also to some other rare earth containing type-I clathrates which are of interest regarding their physical properties, the La-, Pr-, Sm-, and Yb-containing ones. In the case of Yb the growth process was unstable; therefore, we varied the starting composition for optimization of the growth. However, despite our numerous attempts the obtained single crystalline parts were small, sufficient only for single crystal diffraction and EDX measurements. Moreover, they contained inclusions of secondary phases. All grown crystals were investigated by single crystal XRD. The lattice parameters of the grown crystals measured by single crystal X-ray diffraction are given in Table 4. The unit cell dimension is a complex function of the RE ionic radius, the RE content, and the Au content. The lattice parameter of a RE-free clathrate is given for comparison.[15] The refinement supports the location of the RE atoms in the small cages.

Table 4. Lattice Parameters *a* of the Clathrates Single Crystals and for $Ba_8Au_{5.43}Si_{39.8}$[15]

clathrate	*a* (Å)
La-BAS	10.3954(4)[8]
Ce-BAS	10.3863(3)
Pr-BAS	10.3895(3)
Sm-BAS	10.4100(2)
Yb-BAS	10.4152(9)
$Ba_8Au_{5.43}Si_{39.8}$	10.41615(9)[15]

The part crystallized toward the end of the growth typically shows a characteristic striation (Figure 6).

The regularly ordered stripes have the composition $REAu_2Si_2$ or RE_2AuSi_3, both phases rich in RE and Au compared to the clathrate phase. An optical microscopy investigation of the crystal surface in polarized light reveals that the stripes have the same crystallographic orientation, although they are isolated from one another. This indicates that the inclusions are formed epitactically inside the single crystalline matrix. At the end of the growth, the solution accumulates large excess of RE and Au. Apparently, the incorporation of RE(Au) is therefore enhanced at the crystallization temperature, and its excess is released in the form of a RE(Au)-rich phase as the crystal is being cooled to room temperature. An overall composition measurement of the surface with the stripes indicates that the supposed high temperature clathrate phase contains RE in an amount slightly exceeding $x = 2$.

The single crystallinity of the starting and the middle parts was proven by the Laue technique, the phase purity by XRD, SEM, and transmission electron microscopy (ref 8 and Supporting Information to the present paper). EDX and wavelength dispersive X-ray (WDX) analyses show unambiguously the presence of RE elements (see Figure 5b for RE = Ce).

From the single crystal refinement, the compositions of the phases were derived (Supporting Information and Figure 7a), which enables a comparison with that measured by EDX. In order to exclude the influence of inhomogeneity, small single crystalline pieces were selected. They were divided in two parts from which the one part was used in XRD and the other part in the EDX experiment. The compositions obtained by XRD show smaller RE contents and somewhat larger Au contents (Figure 7a). In particular, the difference between the XRD and EDX values for the Yb clathrate is essential. The EDX data are based on rather rich statistics, whereas the XRD measurements were unique for each phase. Another reason for the discrepancy may be a small deviation of the total guest atom stoichiometry from 8. In this case the reduced X-ray scattering of the guest sublattice is interpreted, with the usual constraint $x_{Ba} + x_{RE} = 8$, in favor of a smaller x_{RE}. A total content $x_{Ba} + x_{Ce}$ smaller than 8 was observed by the EDX measurement (Supporting Information).

Trends in Cage Substitution by Elements of the Rare Earth Series. The RE containing clathrates synthesized in ref 8 and here are the first type-I clathrates containing trivalent guest

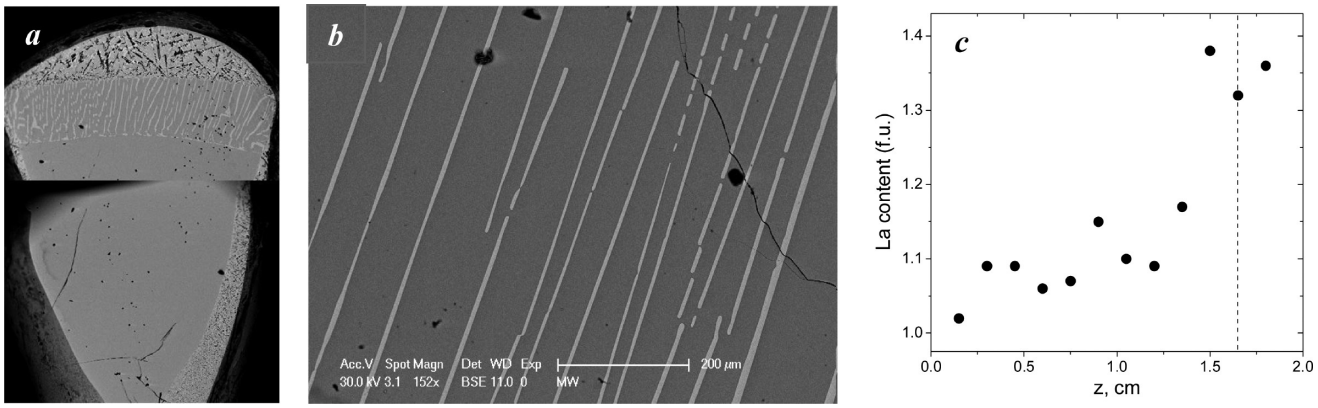

Figure 6. (a, b) Striation of the late-stage part of crystals. Light stripes are inclusions of RE_2AuSi_3- or $REAu_2Si_2$-based phases. (c) Distribution of La in the clathrate phase along a grown crystal. The dashed line marks the boundary with the upper inclusion region.

DOI: 10.1021/acs.cgd.5b00461
Cryst. Growth Des. 2016, 16, 25−33

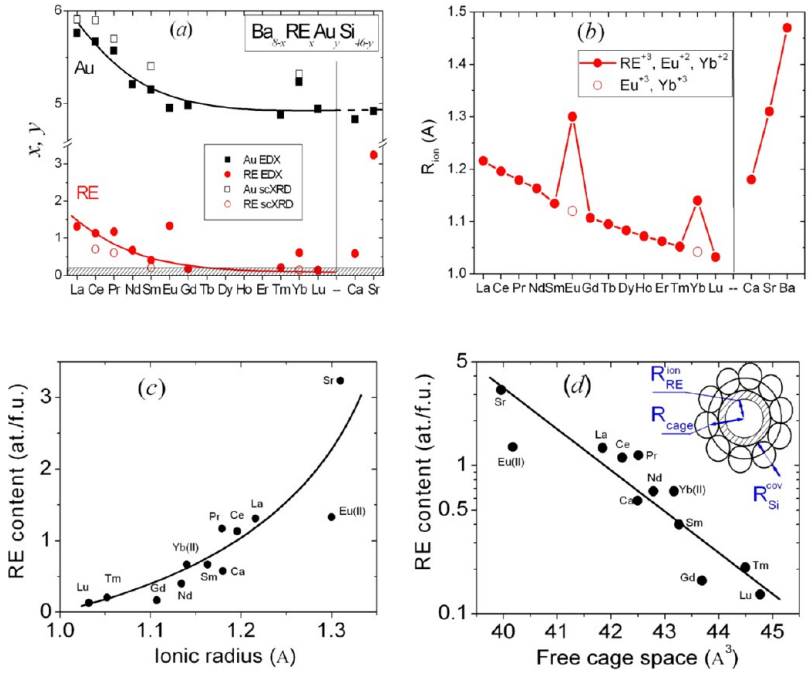

Figure 7. Dependencies in the RE element series: (a) RE and Au contents in type-I clathrates measured by EDX on polyphase samples (full symbols) and by XRD refinement of selected single crystalline samples (empty symbols). The dashed area indicates the RE zero-level of the EDX measurement (see Experimental Section), (b) RE ionic radii (the values for Ca, Sr, and Ba are shown here and further, too);[28] (c) RE content in clathrates (EDX) vs ionic radius of the RE element, (d) RE content in clathrates (log scale) vs free cage space; inset: definition of the free cage space; dashed area illustrates schematically the free cage space.

atoms. Interestingly, the RE content is different for various RE elements. What determines the stability of RE containing clathrate phases? To answer this question, we carried out a systematic study of the substitution ability over the RE element series. For a better overview we widened the scope of RE elements, and for validity of the results the clathrate phases were synthesized under equal conditions, i.e. by the melt synthesis from the starting composition $Ba_6RE_2Au_6Si_{40}$ (see Experimental Section). The compositions were measured by EDX in the clathrate grains of the polyphase materials.

It should be noted that the thermodynamic stability of a phase is meaningful only in relation to the competing neighbor phases. Our XRD investigations show that at least two secondary phases: a phase based on the tetragonal $REAu_2Si_2$ structure and a Si phase appear for all RE elements. The RE content measured by EDX in clathrate phases shows a general tendency to decrease with atomic number, with two distinct anomalies at Eu and Yb (Figure 7a). This behavior reflects the well-known peculiarities of Eu and Yb in the lanthanide series which originate from their ability to exist also in the divalent state (e.g., variation of the ionic radius, Figure 7b). This suggests that Eu and Yb are close to divalent state in the clathrate cages.

The Au content in the RE clathrates shows a general tendency to decrease with the atomic number, in line with the overall trend of the RE content (Figure 7a). This is yet another manifestation of the Zintl concept: a higher content of trivalent guest atoms requires a higher acceptor capacity and thus a higher Au content. In the Eu-clathrate, however, in spite of the anomalously high Eu content, the Au content is not enhanced. This confirms the divalent state of Eu. As Eu donates fewer electrons than the trivalent atoms, less acceptor Au atoms are needed for electron balance. A similar behavior is demonstrated by the definitely divalent Ca- and Sr-substituted clathrates (Figure 7a). Indeed, Eu has been shown to be divalent in the Eu−Ga−Ge and Eu−Ba−Cu−P clathrates.[29,30] The case of Yb is more complex. On the one hand, the increased Yb content is evidence for the larger (divalent) ionic radius; on the other hand, the clearly enhanced Au content is a sign for a valence larger than 2. A valence state of Yb higher than 2 could result in electron correlation effects. This calls for further development of the growth technique to be able to investigate the Yb-containing phase.

The clear correlation between the solubility of the RE element in the clathrate phase and its ionic radius (Figure 7c) leads to the following picture: too much free space in the cage destabilizes the clathrate phase. This is also the reason why the trivalent Ce and La ions, that are smaller than divalent Ba preferentially occupy the 2*a* site in the small cages instead of the 6*d* sites in the larger cages.[8] The observed destabilization effect due to a large free volume is in agreement with previous observations. Among the alkali earth clathrate phases, the phases with the largest ion Ba as the guest atom are by far most abundant.[31] Furthermore, in mixed guest atom alkali or earth alkali clathrates, the smaller atoms occupy the smaller cages and the larger ones the larger cages.[32,33]

Figure 7d reveals the nearly linear dependence of the logarithmic RE content on the free volume of the smaller Si_{20} cage defined as

$$V_{\text{free}} = \frac{4}{3}\pi((\bar{R}_{\text{cage}} - R_{\text{Si}}^{\text{cov}})^3 - (R_{\text{RE}}^{\text{ion}})^3)$$

$$\text{with } \bar{R}_{\text{cage}} = \frac{1}{N}\sum_{i}^{N} R_i$$

where $N = 20$ is the number of the cage atoms in the Si_{20} cage and R_i are distances from the center of the *i*th Si atom to the cage center. $\bar{R}_{\text{cage}} - R_{\text{Si}}^{\text{cov}}$ is the empty cage radius $R_{\text{cage}}^{\text{emty}}$.

DOI: 10.1021/acs.cgd.5b00461
Cryst. Growth Des. 2016, 16, 25−33

Despite the nearly equal ionic radii of Ca and Ce, the solubility of Ca^{2+} is lower than that of the highly charged Ce^{3+}. This may point to a stabilization effect of an enhanced ionic charge in the case of very small ions inside the cages.

Our attempts to synthesize a Ce containing Ge-based clathrate $Ba_{8-x}Ce_xAu_yGe_{46-y}$ failed. No detectable amount of Ce was found by EDX. Figure 8 shows that the solubility of Ce

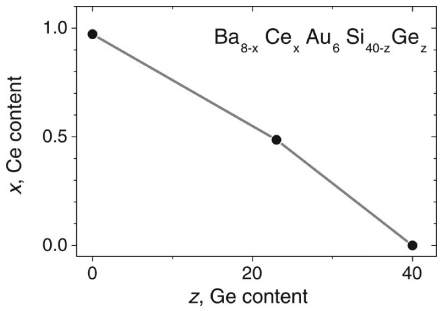

Figure 8. Ce content vs Ge content in the clathrate phase.

decreases roughly linearly with increasing Ge content z in the mixed Si−Ge phase $Ba_{8-x}Ce_xAu_ySi_{46-y-z}Ge_z$. By a full substitution of Si by Ge the average radius of the small cage $\bar{R}_{cage}$ increases from 3.386 to 3.418 Å.[17] However, the empty cage radius ($\bar{R}_{cage} - R^{cov}_{Si(Ge)}$) is smaller for Ge than for Si cages. Thus, the geometrical factor cannot be the only factor determining the stability. We suggest that enhanced covalence due to the more diffuse character of the 4p orbital of Ge compared to the 3p orbital of Si plays a role.

CONCLUSION

Among the transition metal (Au, Pd, Pt) type-I silicon clathrate phases studied in our experiments, the highest substitution level for Ce was found in $Ba_8Au_ySi_{46-y}$. This Ce-containing phase forms only from an off-stoichiometric melt with an excess of Ce and Au. An EDX composition study of various as-crystallized phases revealed rigid correlations between the constituting elements, determined by the tendency of the phase to charge carrier minimization. Overall this behavior is in agreement with the Zintl concept. A closer inspection, however, indicates quantitative deviation from that based on the simple Zintl count. The substitution level of rare earth (RE) elements in $Ba_{8-x}RE_xAu_ySi_{46-y}$ decreases rapidly with the ionic radius of the RE element. We attribute this to a destabilization of the clathrate phase due to increasing free cage space. From the crystal growth experiments, we have indications for an enhanced RE content $x > 2$ in the clathrate phase at increased temperatures, which is, however, unstable at lower temperature. Eu is revealed to be in the divalent state, whereas for Yb an intermediate valence is conjectured. No Ce was detected in the germanium-based clathrate phase $Ba_{8-x}Ce_xAu_yGe_{46-y}$, which is somewhat controversial to the pure geometric approach for explanation of the cage filling.

ASSOCIATED CONTENT

Supporting Information

The Supporting Information is available free of charge on the ACS Publications website at DOI: 10.1021/acs.cgd.5b00461.

Phase analysis of the samples prepared from the starting composition $Ba_6Ce_2TM_6Si_{40}$ (TM = Au, Pt). Typical Laue pattern of a single crystal $Ba_{8-x}La_xAu_ySi_{46-y}$. Summary guest and host local element contents for samples 1−7 (in the clathrate phase). Comparison of the EDX and ICP-MS composition measurements. Comparison of the compositions measured by EDX and that derived from single crystal XRD refinement (PDF)

Accession Codes

CCDC 1441433−1441436 contains the supplementary crystallographic data for this paper. These data can be obtained free of charge via www.ccdc.cam.ac.uk/data_request/cif, or by emailing data_request@ccdc.cam.ac.uk, or by contacting The Cambridge Crystallographic Data Centre, 12, Union Road, Cambridge CB2 1EZ, UK; fax: +44 1223 336033.

AUTHOR INFORMATION

Corresponding Author

*E-mail: andrey.prokofiev@ifp.tuwien.ac.at.

Notes

The authors declare no competing financial interest.

ACKNOWLEDGMENTS

We are grateful to Yu. Grin and co-workers for the elemental analysis of the reference sample. Financial support of the Austrian Science Foundation (project TRP 176-N22) and of the European Research Council (Advanced Grant No. 227378) is gratefully acknowledged. The X-ray centre (XRC) of TU Wien is acknowledged for providing access to the single-crystal diffractometers.

REFERENCES

(1) Slack, G. A. In *Thermoelectrics Handbook*; Rowe, D. M., Ed.; CRC Press: Boca Raton, FL, 2006; Chapter 34 (New materials and performance limits for thermoelectric cooling).

(2) Christensen, M.; Abrahamsen, A. B.; Christensen, N. B.; Juranyi, F.; Andersen, N. H.; Lefmann, K.; Andreasson, J.; Bahl, Ch.R.H.; Iversen, B. B. *Nat. Mater.* **2008**, *7*, 811.

(3) Euchner, H.; Pailhès, S.; Nguyen, L. T. K.; Assmus, W.; Ritter, F.; Haghighirad, A.; Grin, Yu.; Paschen, S.; de Boissieu, M. *Phys. Rev. B: Condens. Matter Mater. Phys.* **2012**, *86*, 224303.

(4) Pailhès, S.; Euchner, H.; Giordano, V. M.; Debord, R.; Assy, A.; Gomès, S.; Bosak, A.; Machon, D.; Paschen, S.; de Boissieu, M. *Phys. Rev. Lett.* **2014**, *113*, 025506.

(5) Saramat, A.; Svensson, G.; Palmqvist, A. E. C.; Stiewe, C.; Mueller, E.; Platzek, D.; Williams, S. G. K.; Rowe, D. M.; Bryan, J. D.; Stucky, G. D. *J. Appl. Phys.* **2006**, *99*, 023708.

(6) Anno, H.; Hokazono, M.; Kawamura, M.; Nagao, J.; Matsubara, K. Presented at the 21st International Conference on Thermoelectrics (ICT2002), Long Beach, CA, USA, August 25−29, 2002; p 77.

(7) Paschen, S. In *Thermoelectrics Handbook*; Rowe, D. M., Ed.; CRC Press, Boca Raton, FL, 2006; Chapter 15 (Thermoelectric aspects of strongly correlated electron systems).

(8) Prokofiev, A.; Sidorenko, A.; Hradil, K.; Ikeda, M.; Svagera, R.; Waas, M.; Winkler, H.; Neumaier, K.; Paschen, S. *Nat. Mater.* **2013**, *12*, 1096.

(9) Krause, L.; Herbst-Irmer, R.; Sheldrick, G. M.; Stalke, D. *J. Appl. Crystallogr.* **2015**, *48*, 3.

(10) Sheldrick, G. M. *Acta Crystallogr., Sect. A: Found. Crystallogr.* **2008**, *64*, 112.

(11) Laugier, J. Bochu, B. LMGP-Suite of Programs for the interpretation of X-ray Experiments. ENSP/Laboratoire des Matériaux et du Génie Physique, BP 46. 38042 Saint Martin d'Hères, France; www.inpg.fr/LMGP and http://www.ccp14.ac.uk/tutorial/lmgp/.

(12) Degen, T.; Sadki, M.; Bron, E.; König, U.; Nénert, G. *Powder Diffr.* **2014**, *29* (Suppl. 2), S13.

(13) Schäfer, H. *Annu. Rev. Mater. Sci.* **1985**, *15*, 1.

(14) Wang, F.; Miller, G.J. *Inorg. Chem.* **2011**, *50*, 7625−7636.

DOI: 10.1021/acs.cgd.5b00461
Cryst. Growth Des. 2016, 16, 25−33

(15) Aydemir, U.; Candolfi, C.; Ormeci, A.; Oztan, Y.; Baitinger, M.; Oeschler, N.; Steglich, F.; Grin, Yu. *Phys. Rev. B: Condens. Matter Mater. Phys.* **2011**, *84*, 195137.
(16) Kasper, J. S.; Hagenmüller, P.; Pouchard, M.; Cros, C. *Science* **1965**, *150*, 1713.
(17) Zeiringer, I.; Chen, M. X.; Grytsiv, A.; Bauer, E.; Podloucky, R.; Effenberger, H.; Rogl, P. *Acta Mater.* **2012**, *60*, 2324.
(18) Melnychenko-Koblyuk, N.; Grytsiv, A.; Rogl, P.; Bauer, E.; Lackner, R.; Royanian, E.; Rotter, M.; Giester, G. *J. Phys. Soc. Jpn.* **2008**, *77*, 54.
(19) Mayer, I.; Cohen, J.; Felner, I. *J. Less-Common Met.* **1973**, *30*, 181−184.
(20) Gordon, R. A.; Warren, C. J.; Alexander, M. G.; DiSalvo, F. J.; Pöttgen, R. *J. Alloys Compd.* **1997**, *248*, 24−32.
(21) Gribanov, A. V.; Seropegin, Y. D.; Tursina, A. I.; Bodak, O. I.; Rogl, P.; Noël, H. *J. Alloys Compd.* **2004**, *383*, 286−289.
(22) Kitagawa, J.; Muro, Y.; Takeda, N.; Ishikawa, M. *J. Phys. Soc. Jpn.* **1997**, *66*, 2163.
(23) Kawaguchi, T.; Tanigaki, K.; Yasukawa, M. *Phys. Rev. Lett.* **2000**, *85*, 3189.
(24) Pacheco, V.; Carrillo-Cabrera, W.; Tran, V. H.; Paschen, S.; Grin, Yu. *Phys. Rev. Lett.* **2001**, *87*, 099601.
(25) Kawaguchi, T.; Tanigaki, K.; Yasukawa, M. *Phys. Rev. Lett.* **2001**, *87*, 099602.
(26) Matta, C. F.; Boyd, R. J. *The Quantum Theory of Atoms in Molecules: From Solid State to DNA and Drug Design*; John Wiley & Sons: New York, 2007.
(27) Zhang, H.; Borrmann, H.; Oeschler, N.; Candolfi, C.; Schnelle, W.; Schmidt, M.; Burkhardt, U.; Baitinger, M.; Zhao, J.-T.; Grin, Y. *Inorg. Chem.* **2011**, *50*, 1250−1257.
(28) Shannon, R. D. *Acta Crystallogr., Sect. A: Cryst. Phys., Diffr., Theor. Gen. Crystallogr.* **1976**, *32*, 751−767.
(29) Paschen, S.; Carrillo-Cabrera, W.; Bentien, A.; Tran, V. H.; Baenitz, M.; Grin, Yu.; Steglich, F. *Phys. Rev. B: Condens. Matter Mater. Phys.* **2001**, *64*, 214404.
(30) Kovnir, K.; Stockert, U.; Budnyk, S.; Prots, Y.; Baitinger, M.; Paschen, S.; Shevelkov, A. V.; Grin, Yu. *Inorg. Chem.* **2011**, *50*, 10387.
(31) Cordier, G.; Woll, P. *J. Less-Common Met.* **1991**, *169*, 291.
(32) Schäfer, M. C.; Bobev, S. *Inorganics* **2014**, *2*, 79.
(33) Böhme, B.; Aydemir, U.; Ormeci, A.; Schnelle, W.; Baitinger, M.; Grin, Yu. *Sci. Technol. Adv. Mater.* **2007**, *8*, 410.

DOI: 10.1021/acs.cgd.5b00461
Cryst. Growth Des. 2016, 16, 25−33